Journal of Polymer Science

WILEY

JOURNAL OF POLYMER SCIENCE

RESEARCH ARTICLE OPEN ACCESS

Load-Induced Shear Band Formation in Microscale Epoxy Materials

Janina Mittelhaus[1] | Julian Konrad[2] | Julius Jacobs[1] | Phil Röttger[1] | Robert Meißner[2,3] | Bodo Fiedler[1]

[1]Hamburg University of Technology, Institute of Polymers and Composites, Hamburg, Germany | [2]Hamburg University of Technology, Institute for Interfacial Physics and Engineering, Hamburg, Germany | [3]Helmholtz-Zentrum Hereon, Institute of Surface Science, Geesthacht, Germany

Correspondence: Janina Mittelhaus (janina.mittelhaus@tuhh.de) | Julian Konrad (julian.konrad@tuhh.de)

Received: 12 December 2024 | **Revised:** 11 February 2025 | **Accepted:** 26 February 2025

Funding: This research received funding from Grant No. 525597740 provided by the Deutsche Forschungsgemeinschaft (DFG, German Research Foundation). Publishing fees are supported by the Funding Programme Open Access Publishing of Hamburg University of Technology (TUHH).

Keywords: ductility | epoxy films | infrared spectroscopy | molecular dynamics | shear bands

ABSTRACT

Thermosetting polymer thin films exhibit distinct mechanical behaviors at the microscopic scale compared to bulk materials. Experimental results reveal significant necking and unexpected shear band formation under tensile load. This study investigates the mechanisms underlying shear band formation in epoxy resin systems composed of bisphenol-diglycidyl-ether and diamines. Mechanical testing methods, including creep, relaxation, and cyclic testing, as well as ex situ and in situ high-resolution infrared (IR) spectroscopy, are used synergistically with quantum mechanical calculations to elucidate the underlying molecular mechanisms. Additionally, molecular dynamics (MD) simulations on a nanoscale model explored the (visco-)plastic behavior and network strain in epoxies. Our findings reveal a strong correlation between shear band formation and shifts in IR spectra, specifically the redshift of *para*-phenylene and the blueshift of out-of-plane vibrations of aromatic moieties. These shifts are attributed to load-induced aromatic stretching in the polymer backbone. The robust agreement between experimental data and simulation results supports these observations at both the atomic and nanoscale. These insights enhance the understanding of epoxy resin mechanics, potentially informing the design of advanced composite materials.

1 | Introduction

Fiber-reinforced polymers (FRPs) are widely used in industrial applications that require high mechanical performance and low weight, such as the wind energy, automotive, and aerospace industries. FRP structures consist of oriented fibers embedded in a matrix material, which is often an epoxy resin system. This results in zones of interconnected matrix materials in the (sub-) micrometer range, such as resin-rich zones between fibers within a prepreg of 1–25 μm and interlayer distances between reinforcing prepregs or layers of 10–200 μm [1]. In practice, the characterization of such matrix materials is typically performed using macroscopic test volumes specified in standardized test methods. However, using bulk mechanical parameters from standard specimens for microscale modeling of composite materials often leads to discrepancies between modeled and observed behavior, potentially due to differences in the mechanical behavior of the microscopic matrix compared to macroscopic bulk specimens [1–9]. More fundamental insights into the micromechanical properties and deformation behavior of the thermoset matrix as a microcomponent of composites are therefore a crucial aspect for the further optimization of polymer composites.

Fourier transform infrared (FTIR) spectroscopy and microscopy are well-established techniques to analyze materials under load, revealing deformation mechanisms at a molecular level and

Janina Mittelhaus and Julian Konrad contributed equally to this study.

providing information about load-induced molecular changes [10, 11]. These techniques have been applied to various materials, including fibers made of aramid [12–14], poly(*p*-phenylene-2,6-benzobisoxazole) (PBO) [15], carbon [16, 17], polyethylene terephthalate (PET) [18], and biomaterials such as cellulose [19–23], silkworms [24], and spider silk [25], as well as composite materials [2, 3, 8, 26–30]. While IR experiments provide insights into molecular and atomic level phenomena, they are usually limited in spatial or temporal resolution. A combination of experimental and computational approaches offers the possibility to elucidate and understand fundamental mechanisms in more detail. For example, recent studies have shown that molecular dynamics simulations supported by quantum mechanical calculations can characterize processes related to elasticity [31–33], plasticity [34, 35], or fracture across multiple time and length scales in epoxies [36–38]. Changes in the network structure at an epoxy interface, in the form of molecular orientations, have been observed as well recently in such simulations [39–43]. Such changes at the interface are particularly important for thin-film thermosets under stress, as their surface-to-volume ratio is significantly larger compared to bulk samples. Thus, thin film epoxy specimens provide a means to investigate and disentangle molecular effects, such as bond stretching or intermolecular interactions, related to the observed plasticity under mechanical loading that are also likely to be important in FRP using both experimental and atomistic simulation methods. Consequently, and building on previous works [44, 45] that have applied FTIR to the study of cross-linked epoxies, this work seeks to further exploit experimental as well as simulation approaches to understand in more detail the molecular mechanisms, for example, the causes of peak shifts in the surprisingly large shear bands formed in thin film epoxies, which are known to be a rather brittle material when thicker.

The scope of the investigation ranges from atomistic scales, in relation to Badger's rule, to nanoscale structural features and macroscopically observable patterns, ultimately drawing a multiscale picture of this particular mechanical behavior. Additionally, this work seeks to bridge the gap between micro- and macroscopic understandings of epoxy resin behavior, providing a comprehensive model that can inform the design and optimization of advanced FRP materials.

2 | Materials and Methods

2.1 | Material Preparation and Mechanical Testing

In our previous study, a new infusion manufacturing process was developed and optimized to produce thermoset films with a defined thickness [44]. Epoxy thin-film samples are prepared with a low viscosity resin system consisting of EPIKOTE Resin MGS RIMR 135, which is based on diglycidyl ether of bisphenol A (DGEBA), combined with a liquid aliphatic diamine hardener, EPIKURE Curing Agent MGS RIMH 137 (Westlake, International: USA/Europe) is used. Both components are mixed in a weight ratio of 100:30 in a mixer (SpeedMixer DAC 150.1 FVZ) at 3500 rpm for 5 min. The backbone of the epoxy or DGEBA contains aromatic rings, or more precisely *para*-phenylene groups, as shown in Figure 1. By using the developed manufacturing method, epoxy films with a thickness of 15.8 ± 2.0 and 32.4 ± 2.0 μm are manufactured.

Before mechanical testing, all film samples are analyzed by IR spectroscopy and microscopy to identify the initial IR signal. After the manufacturing, the thickness of the films is verified, and the utilized dogbone geometry (see Figure 2) is obtained by punching. All mechanical tests are carried out at room temperature with a Deben tensile microstage *MT200* and a 20 N load cell. The strain is determined by the cross-head displacement, and the clamping jaws are torqued with 0.4 Nm. The Deben stage is controlled by the corresponding Deben software V 6.10. After sample clamping, the Deben microtest stage is installed in the IR sample chamber together with an already clamped film sample. The geometric dimensions of geometry A and B deviate from the established standard DIN EN ISO 527-3, as they are predefined by the used Deben microtest stage. Geometry B is more suitable for the shear band analysis with IR under load since the necking and shear band formation take place in the specimen's center due to the reduced width there. The in situ IR tracking is more feasible with geometry B, but geometry A corresponds more to the standard dogbone shape. Thus, samples with both geometries are mechanically tested. Samples with geometry A are investigated by ex situ microscopy, and for the in situ IR spectroscopy analysis, samples with geometry B are used.

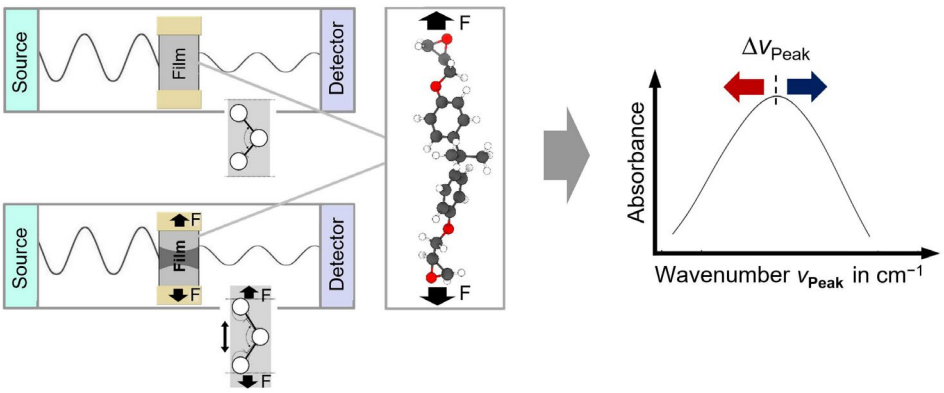

FIGURE 1 | Schematic overview of in situ setup (mechanical testing and IR). The molecular structure of DGEBA changes due to mechanical load introduction and thus causes variations in the IR spectra. Resulting spectral modifications can be peak shifts ($\Delta\nu_{peak}$) to higher or lower peak wavenumbers.

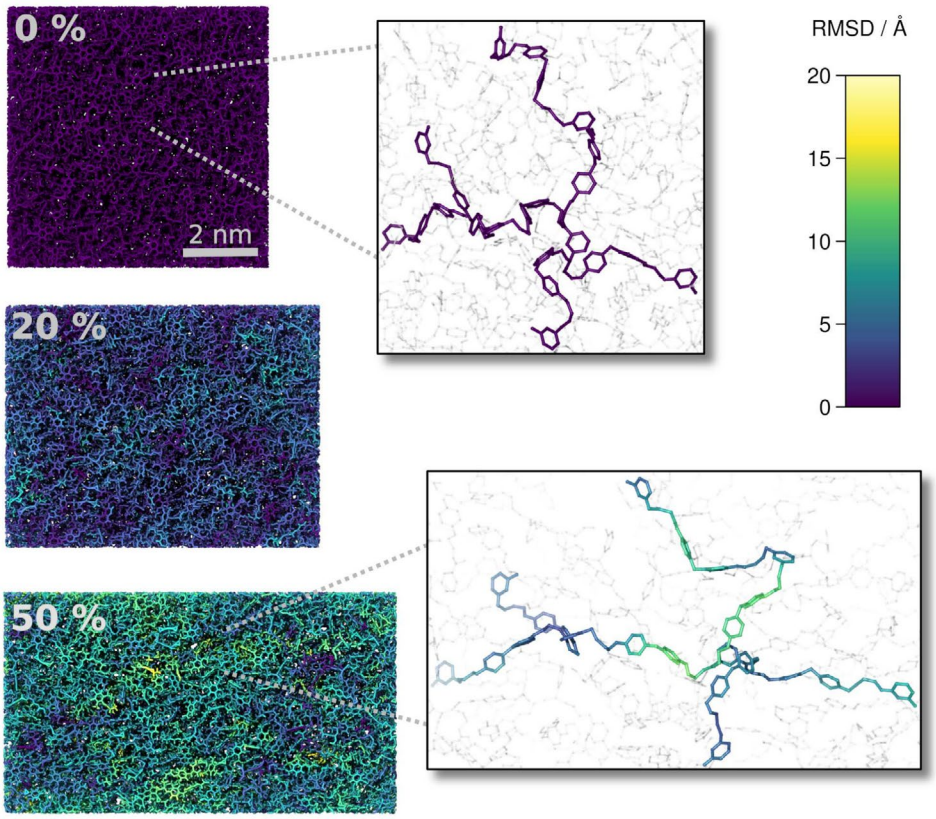

FIGURE 2 | To illustrate molecular reorientation, snapshots for deformations of 0%, 20%, and 50%, respectively, are presented. The coloring corresponds to the RMSD value, which represents the deviation of atomic positions from the ideal elastic deformation. The close-up views highlight the necessity of untwisting molecular chains for network elongation. Furthermore, it is evident that diverse nano-scale domains develop throughout the deformation process, ultimately merging and resulting in the overstretching of the entire network and subsequent fracture.

In situ creep tests are carried out according to EN ISO 899-1 to analyze the impact of time on the microstructural changes under constant mechanical stress. The creep tests are performed at stress levels of approximately 56 MPa (80% of Ultimate Tensile Strength (UTS) [44]) for 30 μm thick epoxy films and at approximately 50 MPa (70% of UTS [44]) for films with a thickness of 15 μm. Stress is generated with a cross head speed or loading rate of 1 mm/min at the beginning of the creep test. With an initial clamping distance of 17.5 mm and a maximum distance of 20.5 mm between the outer edges of the clamping jaws, the maximum nominal strain achievable by the Deben stage is about 18%.

Both sample geometries are investigated under creep loading (see Figure 2). The gauge length of the specimens is 10 mm (for geometry A) or 2 mm (for geometry B). This results in a strain rate of $1.667 \times 10^{-3} s^{-1}$ (sample geometry A) or $8.33 \times 10^{-3} s^{-1}$ (sample geometry B) at the beginning of the creep test. Relaxation tests are carried out according to DIN 53441 to investigate the molecular relaxation processes due to a constant strain application. Epoxy films with thicknesses around 30 μm and geometry B (see Figure 2) are investigated in relaxation tests. The strain value is set up to 4% which corresponds to a strain value above the yield strain. The crosshead speed to reach the defined strain value is 1 mm/min.

Epoxy films with thicknesses around 30 μm and geometry B (see Figure 2) are tested under cyclic loading. The maximum stress used is approximately 70% of the UTS of the corresponding tensile tested epoxy films, which corresponds to approximately 50 MPa. The minimum stress is set to 0 MPa. This results in a mean stress of 25 MPa and a pure tensile swelling load with a stress ratio $R = 0$. The stresses are kept constant for 10 min and applied at a crosshead speed of 1 mm/min. A holding time of 10 min for the maximum and minimum stresses is selected in such a way that the epoxy film specimens have time to respond to the applied load.

All mechanically tested specimens are additionally examined using photoelasticity to further visualize shear bands and necking zones. Polarized light is used to study the stress distribution in the translucent epoxy films. A Keyence VHX-6000 microscope is used with a VH-Z20 objective and a polarization adapter after mechanical loading and before IR analysis. The photoelastic measurement is performed in transmitted light mode, that is, the translucent and deformed epoxy film is positioned on a glass sample holder.

2.2 | Ex Situ and In Situ Infrared Analysis

All IR spectra are recorded in the mid-infrared (MIR) range of 4800 to 500 cm^{-1} in transmission mode with a resolution of 1 cm^{-1}. Before a sample measurement is started, 40 background spectra are taken from the atmospheric environment in the sample chamber without a specimen. In the in situ IR method, spectra are recorded during mechanical testing and the peak wavenumbers ν_{peak} of load-bearing bonds are tracked. The schematic setup is shown

in Figure 1. In situ IR measurements are performed with a Bruker TENSOR II instrument and OPUS 7.5 software. A single spectrum is recorded every 7 s at a defined and fixed position of the film sample center (circular area with a diameter of 5 mm). This allows the wavenumbers of selected and stress-sensitive molecular bonds or vibrational modes to be tracked over time during mechanical testing. For in situ IR mechanical tests, the Deben tensile microstage is used for the different mechanical tests and inserted into the Tensor II sample chamber. By applying a peak fitting method, peaks of load-bearing bonds in each recorded spectrum during the mechanical test, are analyzed and spectral changes due to the mechanical load application, for example, peak shifts, can be detected [45]. The ex situ analysis, before and after the mechanical loading is performed with a HYPERION 2000 infrared microscope from Bruker with very high spatial resolution. A × 15 objective is selected to investigate a sample area of a square pixel with a size of $165 \times 165\ \mu m^2$. Thus the resolution is much higher since the investigated sample area is significantly reduced compared to the in situ IR measurements with a TENSOR II spectrometer (circular sample area with a diameter of 5 mm) and the distinguishing of the deformed and non-deformed sample region is possible.

Utilizing the IR microscope, the measurement distance is set to 165 µm. A comprehensive, gapless grid IR measurement was conducted across the entire deformed specimen. This grid-based approach allowed for a detailed analysis of the molecular interactions and structural changes within different domains of the material.

2.3 | Quantum and Molecular Mechanics Methods

The IR spectra of the resin molecules are computed quantum mechanically using GAUSSIAN [46] under the B3LYP/6-311+G** method. Prior to vibrational analysis, the structures are initially minimized using the OPLS-AA force field [47] and further optimized quantum mechanically. The main focus is on the epoxy molecules of BFDGE (diglycidyl ether of bisphenol F) and DGEBA. The molecules exhibit only a variance in two methyl groups between the aromatics, resulting in similar elastic properties and mechanical behavior [48]. Additionally, a single linked species of BFDGE and DETDA (diethyltoluoldiamin) is investigated within the context of a complete epoxy network unit.

For our computational investigations of nano-scale phenomena, an epoxy resin model previously established and characterized [33, 35, 37, 41, 43, 49] is utilized. This model, representing a cured epoxy resin with a 98% crosslinking degree, comprised 1024 BFDGE and 512 DETDA moieties, resulting in cell dimensions of 8.4 nm. Periodic boundary conditions are applied to simulate bulk behavior. To capture reactive processes such as bond formation and dissociation during tensile deformation, the model is subjected to a reactive force field derived from OPLS-AA [37]. Non-bonded interactions are described by Lennard-Jones potentials with the cutoff at 12 Å and Coulomb contributions by the damped-shifted force approach [50] with a cutoff distance of 10 Å while damping is applied with a factor of $0.1\ Å^{-1}$ [51]. The simulations are performed using the LAMMPS [52] simulation software with a timestep of 0.5 fs. Constant temperature and pressure are maintained utilizing the Nosé-Hoover algorithm [53] with damping factors of 0.1 and 1.0 ps, respectively.

3 | Results and Discussion

Figure 3a shows a photoelastic image of a representative creep-loaded film specimen with a thickness of 30 µm without failing during the mechanical creep loading until a strain of 16%. There are clearly visible shear bands in the deformed and necked epoxy specimen region of all creep, relaxation and cyclic tested film specimens, which is unusual for rather brittle thermoset materials in general and for epoxy resins in particular. Regions of visco-plastic deformation due to shear stress are actually a typical example of the non-linear deformation behavior of thermoplastics. The shear bands in thermoplastic materials represent an inhomogeneity of orientation and usually occur at an angle of ± 45° to 55° to the direction of loading [54]. The formation of shear bands in thermoplastics is favored by a stress-induced decrease in volume [55]. However, these explanations cannot be directly transferred to thermosets, since they are highly crosslinked and slippage of macromolecular chains in a comparable manner is not familiar for epoxy resins.

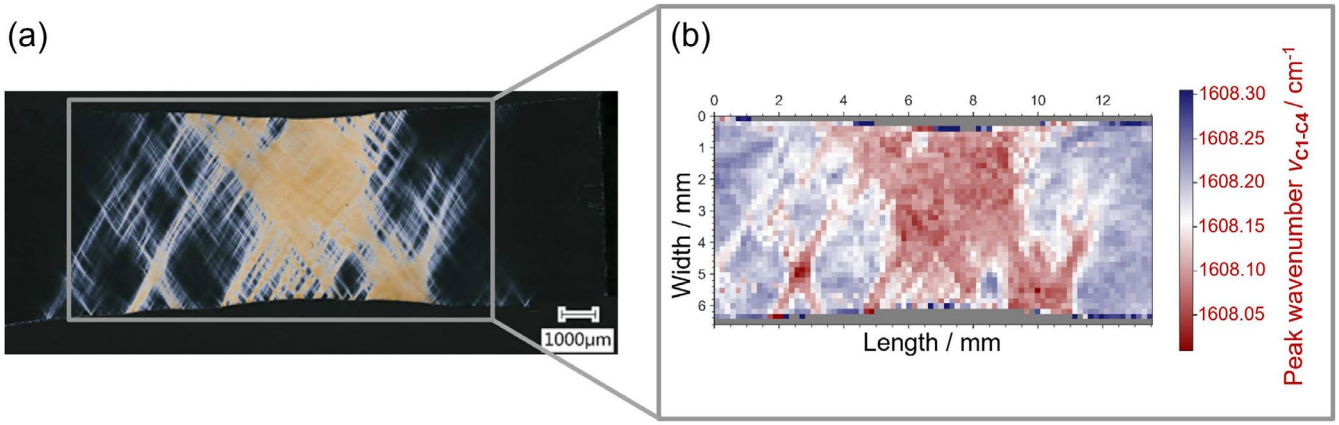

FIGURE 3 | Correlation of a photoelastic image (a) and ex situ IR microscope results (b) of a representative creep-loaded film specimen of type A with a thickness of 30 µm without failing during the mechanical creep loading (maximum elongation of 16%). Each pixel with a size of 165 × 165 µm is a measurement point and correspond to a spectrum. All recorded spectra are evaluated regarding the aromatic peak wavenumber $\nu_{C_1-C_4}$. Depending on the value of $\nu_{C_1-C_4}$, each pixel is colored.

Infrared analysis is a valuable method for investigating the molecular mechanisms and causes of macroscopically visible shear bands. One essential requirement for ex situ and in situ IR measurements on loaded epoxy films is that vibrational modes of stress-sensitive bonds appear distinctly as well-resolved peaks in the spectrum, without overlapping neighboring peaks and with appropriate intensity. Thus, films with thicknesses around 15 μm are analyzed to reduce the high absorbance of some vibrational modes.

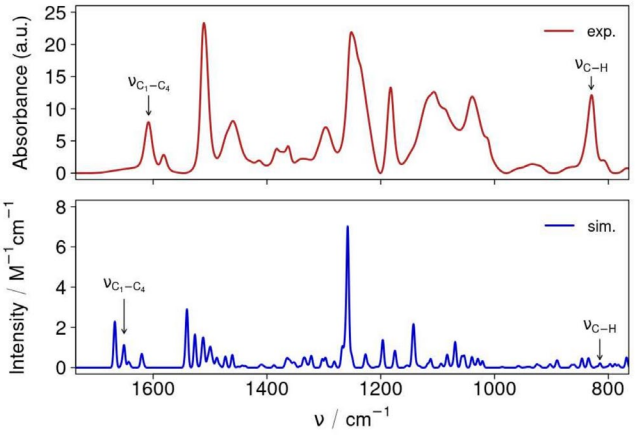

FIGURE 4 | Recorded IR spectrum of a representative as-produced epoxy film sample with a thickness of 30 μm (top). Calculated IR spectrum of a BDFGE molecule, linked between two DETDA moieties (bottom).

Furthermore, extracting load-induced peak shifts from complex spectra, where peaks may shift in relation to each other and collectively affect total absorbance, poses a significant challenge. In contrast, quantum mechanically calculated IR spectra typically allow precise assignment of peaks to specific vibrational modes of functional chemical groups. Thus, mechanical loads can be precisely examined with atomic-level detail, supplementing experimental findings.

An IR spectrum of a representative as-produced epoxy film sample with a thickness of 30 μm, along with the calculated IR spectrum of a single polymer chain consisting of a BFDGE moiety linked between two DETDA units, are depicted in Figure 4. For instance, selected vibrational modes can be assigned to the functional groups of the backbones in the polymer network, such as the in-plane aromatic ring stretching $C_1 - C_4$ at 1608 cm^{-1}. The resolution of individual peaks in the calculated spectrum is significantly higher. The general shift of peaks to lower wavenumbers in the experimental spectrum is attributed to the local electrostatic environment.

Since the *para*-phenylene group is an integral part of the polymer backbone in epoxy resin, the $C_1 - C_4$ in-plane and C—H

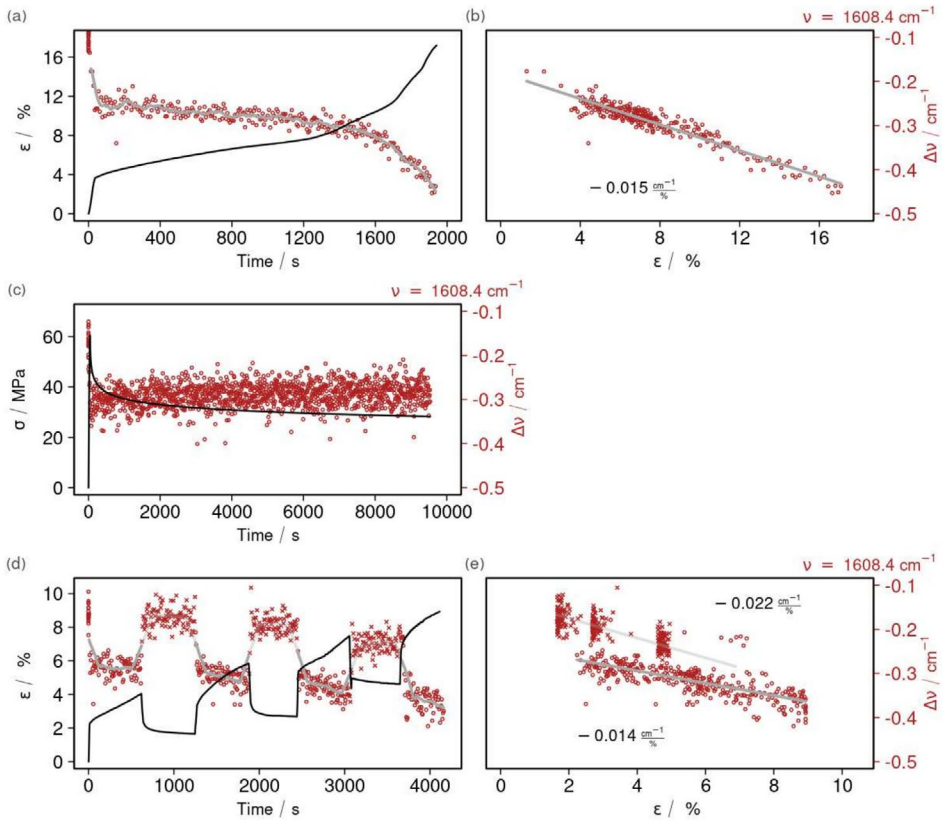

FIGURE 5 | In situ tracking of the aromatic peak wavenumber $\nu_{C_1-C_4}$ around 1608 cm^{-1} over the time for representative film specimens of type B with a thickness of 30 μm during (a) creep at 80% UTS, (c) relaxation at 4% strain, and (d) cyclic loading with $\sigma_{max} = 70\%$ UTS. The corresponding mechanical data is represented by the black lines. The correlation between the wavenumber $\nu_{C_1-C_4}$ and strain during loading is depicted in (b), and during both loading (circles) and unloading (crosses) in (e). The slopes of the linear fits indicate the change in wavenumber per unit strain.

out-of-plane vibrations are mainly investigated in this work. To analyze the molecular mechanisms of the aromatic *para*-phenylene group the aromatic peak wavenumber $\nu_{C_1-C_4}$ at 1608 cm^{-1} is tracked during different mechanical load states during the creep, relaxation and cyclic experiments (see Figure 5). Due to comparatively small changes in the peak wavenumbers peak fitting is performed by approximating Gaussian functions to stress-sensitive peaks from the measured IR raw data [56]. The characteristic features of the distribution like the peak wavenumber of the peak maximum can be extracted. The tracked peak wavenumber of the $\nu_{C_1-C_4}$ is depicted by red dots during the mechanical tests in Figure 5.

It can be seen that a macroscopic material stretching leads to a decrease in the aromatic peak wavenumber $\nu_{C_1-C_4}$. Figure 5a shows the tracked aromatic peak wavenumber during the creep test for a 30 µm thick representative film sample at 56 MPa. For the elastic stretching which occurs in the first creep phase a pronounced shift towards lower aromatic peak wavenumbers $\nu_{C_1-C_4}$ can be found. In the second creep phase with an almost constant strain, only a comparably small aromatic peak shift is observed. In the third creep phase the aromatic peak wavenumber $\nu_{C_1-C_4}$ decreases sharply again as a result of an increased macroscopic material stretching. The strain during creep testing shown in Figure 5b shows that the peak wavenumber $\nu_{C_1-C_4}$ of the aromatic $C_1 - C_4$ stretching can be directly and linearly correlated with the mechanical deformation or the creep strain of the epoxy resin film.

Similarly, in relaxation and cyclic mechanical experiments, the aromatic peak wavenumber can be tracked as shown in Figure 5d,e. In the relaxation experiment a steep decrease in $\nu_{C_1-C_4}$ at the beginning of the experiment and a small increase during molecular stress relaxation processes (see Figure 5c) is observed. The cyclic loading experiments show an overall decrease in $\nu_{C_1-C_4}$ upon mechanical loading and to some extent not a full recovery of the initial peak wavenumber upon unloading and can also be correlated with strain.

The visco-elastic behavior of the material is characterized by reversible and spontaneous changes in bond length and molecular angles. This can be quantified by observing a redshift in stretched bonds during the initial phase of mechanical loading (see Figure 5a,d). In contrast, visco-plastic deformation involves additional, time-dependent phenomena such as bond lengthening, untwisting, unraveling of entanglements, and positional changes of molecular chains within the network. This is evident in Figure 5d. During cyclic testing, the peak wavenumber does not return to its initial value during the unloading cycle due to insufficient time for complete relaxation. Consequently, the material does not fully revert to its previous strain state. This behavior is also reflected in the slope of the linear fit during unloading (crosses), which is approximately $-0.022\ cm^{-1}/\%$ as shown in Figure 5e. A linear fit of the strain versus wavenumber during the loading cycle is also presented. The slope of the loading cycle is approximately $-0.014\ cm^{-1}/\%$, which is comparable to the slope observed in the linear fit for creep loading, as shown in Figure 5b. The visco-plastic and plastic deformation is more common in thermoplastic materials but can occur in thermosets as well [1]. The unraveling of entanglements can allow the bonds to be stretched further. Recognizing these complex molecular behaviors is crucial for understanding the overall mechanical response of epoxy materials. By examining these behaviors, it is possible to gain insights into the fundamental mechanisms driving visco-plastic deformation.

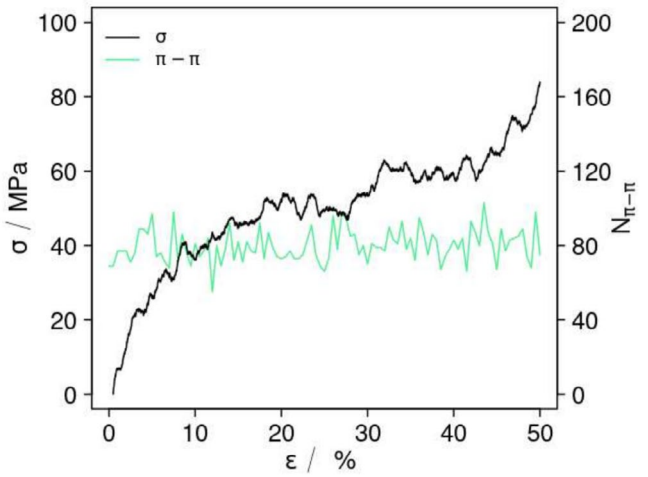

FIGURE 6 | The stress–strain diagram (in black) of the bulk epoxy model at a strain rate of $\dot{\epsilon} = 10^7, s^{-1}$ behaves elastically up to approximately 5% deformation, after which it exhibits plastic deformation. The number of π–π interactions (in green) shows no significant increase or decrease, emphasizing the assumption of the minimal impact of intermolecular interactions on peak shifts under load.

Expanding upon the experimental insights regarding peak shifts within epoxy networks, bulk epoxy composed of BFDGE and DETDA is investigated by simulations. To explore this visco-plastic behavior, molecular dynamics simulations on a nano-scale model are conducted while employing a reactive force field accounting for possible bond dissociation. This model displays significant consistency in terms of mechanical properties, as evidenced in the references [37, 49]. Tensile deformation is carried out at a strain rate of $\dot{s} = 0.084\ \frac{m}{s}$ ($\dot{\epsilon} = 10^7\ s^{-1}$) until reaching a deformation of $\epsilon = 50\%$. The chosen strain rate is necessary due to the limited time scales in molecular dynamics. While higher than experimental rates, it remains slow for atomistic modeling. As demonstrated in previous works [37, 49], stress relaxation occurs within 10 ns, allowing the strain-rate dependent stress to relax sufficiently. The resulting tensile stresses align well with experimental values, indicating consistency despite the strain rate difference. The stress–strain diagram (in black), depicted in Figure 6, illustrates elastic behavior up to approximately 5% deformation, transitioning thereafter to plastic deformation, as indicated by the deviation from linearity in the stress curve. Additionally, π–π interactions (depicted as green curve in Figure 6), encompassing face–face and face–edge interactions between the aromatic *para*-phenylene groups, are investigated to assess their potential influence on the spectral characteristics of nonbonding interactions. The definitions for determining π–π interactions can be found in the Supporting Information: Section S1.3. Throughout the deformation process up to 50%, a consistent number in the π–π interactions is observed, with no significant increase or decrease detected. However, fluctuations due to dynamic processes within the simulation are noticeable, as shown in Figure 6, indicating a change in structure without a quantitative increase in π–π interactions.

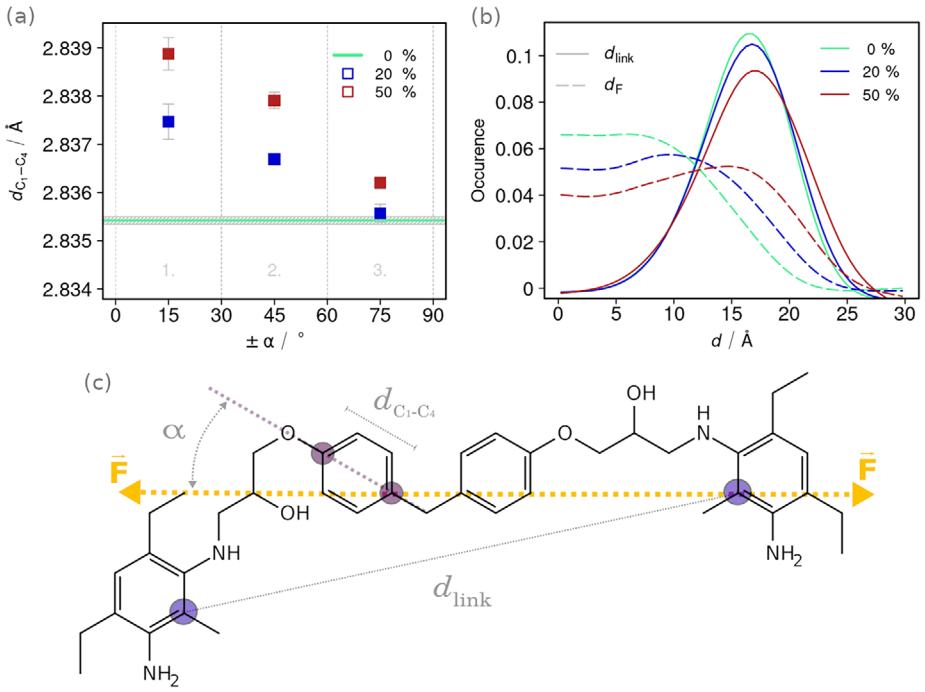

FIGURE 7 | In order to elucidate intra-molecular strain mechanisms (a), an analysis is presented for the distance $d_{C_1-C_4}$ (c) and three angle intervals based on orientation relative to the pulling direction (illustrated in orange), denoted by α are defined. The distances $d_{C_1-C_4}$ are considered for strains of 0%, 20%, and 50%, respectively. The observations reveal an increment in $d_{C_1-C_4}$ with increasing deformation, with a notably pronounced augmentation dependent on the angle relative to the pulling direction. The network strain (b) is delineated and captured by the distance d_{link} (c) between DETDA molecules of the hardener (depicted in purple) within the polymer network. The frequency profiles illustrate a rising network strain attributed to the increase in distances d_{link} (solid lines) between network nodes (DETDA molecules) as tension progresses depicted with coloring from green to blue to red. This is accompanied by a notable elevation in the portion aligned with the direction of tension d_F (dashed lines), indicative of molecular chain elongation induced by strain.

In order to obtain comprehensive statistics for intra-molecular mechanisms under load, quasi-static relaxation runs are performed over 10 ns at strains of $\epsilon = 0\%$, 20% and 50%, which also promote visco-elastic and visco-plastic relaxation processes. This allows to extrapolate stresses for $t \to \infty$ via first-order kinetic fits and reduce strain rate dependent intra-molecular stresses. As a result, $\sigma_{t\to\infty}(20\%) = 35\,\text{MPa}$ and $\sigma_{t\to\infty}(50\%) = 58\,\text{MPa}$ is obtained, comparable to the experimental values. Relaxed structures are employed as starting points for simulations lasting 25 ps under constant volume conditions, facilitating a detailed analysis of the orientation and displacement of the aromatic rings with respect to the C_1 and C_4 atoms. A sampling frequency of 10 fs is chosen to ensure the independence of each individual measurement, validated by the auto-correlation function. The analysis focused on the distance $d_{C_1-C_4}$ and the orientation relative to the direction of tension, denoted by α, as illustrated in Figure 7 (bottom). The distributions of the considered distances are categorized into three angle intervals: (1) aligned with the direction of tension, (2) inclined to it, and (3) orthogonal to the direction of tension, determined according to $\alpha < 30^\circ$, $30^\circ \geq \alpha < 60^\circ$, and $\alpha \geq 60^\circ$, respectively. In Figure 7 the distances are presented for the strains of 0%, 20% and 50%, respectively. Overall, there is a trend of increasing $d_{C_1-C_4}$ with increasing displacement. When comparing the distances between C_1 and C_4 within the smallest angle interval ($0^\circ \leq \alpha < 30^\circ$), an increase of 0.004 Å for the system at $\epsilon = 50\%$ from the initial value of 2.8355 Å can be noted. Despite the marginal increase, the error margins derived from pulling in the three spatial directions imply significance. Aromatic rings aligned with the direction of tension experience the most substantial elongation compared to those oriented perpendicular to it. Hence, elongation is associated not only with the alignment of the aromatic rings depicted by α, but also with stretching within these rings, specifically $d_{C_1-C_4}$. Therefore, it can be asserted that visco-elastic and visco-plastic deformation modes induce elongation of the *para*-phenylene group in the tensile direction, consequently causing a redshift according to Badger's rule, consistent with experimental data. The empirical Badger's rule, originally made for describing diatomic molecules, correlates the force constant (k) with the bond length (r) and the element-dependent equilibrium distance (r_0) [57–59], $k^{-\frac{1}{3}} \propto (r - r_0)$. This rule indicates an inverse relationship between bond length and force constant. When a bond undergoes stretching due to applied load, the decrease in the force constant manifests as a redshift in the corresponding stretching vibrational mode or peak wavenumber [10, 60]. Although originally formulated for diatomic and small molecules, the general correlation between bond length, force constant, and vibrational frequency or wavenumber applies surprisingly to a wide range of materials, including wood and cellulose [11, 61], phenylene terephthalamide (PET) [12], polypropylene (PP) [62], and epoxy resin [44]. Moreover, the theory of adiabatic internal coordinate modes (AICoMs) has been employed to establish bond length–bond stretching force constant relationships, extending the applicability of this correlation to polyatomic systems as well, provided that certain prerequisites are met [63]. Specifically, the bond stretching force constant

must correspond to a local mode derived using AICoMs, and the relationship must account for effective bond lengths, corrected for atomic size, charge, and spin multiplicity.

Given that the previous results operate on a highly atomic level, where mechanisms unfold within a few angstroms, the influence of nm-sized structures on individual molecule fragments is investigated in the following. In this context, the epoxy network is categorized into nodes representing the DETDA molecules and connections between them when linked by BFDGE molecules. The distance vector between these nodes, d_{link} is depicted in Figure 7 on the bottom and is further analyzed in terms of magnitude and orientation relative to the direction of tension. The frequency distribution reveals that with increasing deformation, the distance $d_{\text{link}} = \| d_{\text{link}} \|$ increases (solid lines), indicating stretching of the entire network structure. Moreover, it can be observed that the proportion of the distance aligned with the direction of tension d_{F} experiences the most significant increase (dashed lines), further highlighting the alignment and stretching of the network structure in the direction of tension. This mechanism on the nanometer scale subsequently causes the *para*-phenylene group to align and stretch during deformation, thereby facilitating the observed redshifting in experiments.

Considering the complex nature of the alignment and stretching process of the network structure, the differences within this structure are analyzed. Particularly intriguing are the regions of (visco-)plastic deformation. To quantify this, the root-mean-square deviation (RMSD) value is calculated, which represents the deviation of each atom at t_ϵ from the ideal elastic displacement. The ideal elastic position $r_{i,\text{elastic}}$ of atom i is given by:

$$r_{i,\text{elastic}} = r_i(t_0) \cdot \begin{pmatrix} \epsilon_x & 0 & 0 \\ 0 & \sqrt{\frac{1}{\epsilon_y}} & 0 \\ 0 & 0 & \sqrt{\frac{1}{\epsilon_z}} \end{pmatrix} \tag{1}$$

where $r_i(t_0)$ is the initial position of atom i, and ϵ_x, ϵ_y, and ϵ_z are the principal strain components along the respective coordinate axes. This matrix represents the deformation transformation when the material is pulled in the x-direction. The RMSD value for each atom is then computed as: $\text{RMSD}_i(t_\epsilon) = \sqrt{\left| r_i(t_\epsilon) - r_{i,\text{elastic}} \right|^2}$ where $r_i(t_\epsilon)$ is the actual position of atom i at strain t_ϵ. Higher RMSD values indicate stronger deviations from purely elastic deformation, highlighting regions of plastic deformation. In Figure 8, snapshots are presented colored according to the RMSD value, representing plastic deformation for different strains on the left-hand side. A general increase in plastic deformation is visible throughout the entire polymer network. As elongation progresses from 0% to 20%, the initiation of plastically deformed domains is evident. Subsequently, even larger domains exhibiting more pronounced plastic deformation emerge with further deformation up to 50%. The underlying mechanism is substantially illustrated by close-up views of the backbone atoms, depicting the untwisting, unraveling of entanglements and stretching of molecules. The stretching process is limited to the maximum length of the untwisted molecule. As deformation continues, leading to bond rupture and material failure, it becomes crucial to understand the mechanisms underlying shear band formation and their specific impact on different domains.

To further explore these domains, particularly in relation to shear band formation, a representative creep-loaded and deformed film specimen with a thickness of 30 μm is analyzed, as shown in Figure 3a.

Analyzing this with the grid-based approach creates an aromatic peak wavenumber visualization for the entire deformed sample and can be seen in Figure 3b. Regarding the wavenumber value of $\nu_{C_1-C_4}$, each measurement point gets a defined color.

The sample regions with reduced aromatic peak wavenumbers are colored in red. It is unambiguous, that the recorded spectra with an aromatic peak redshift towards lower wavenumbers can only be detected in shear bands. In the optical non-deformed sample region (black colored regions in the photoelastic image,

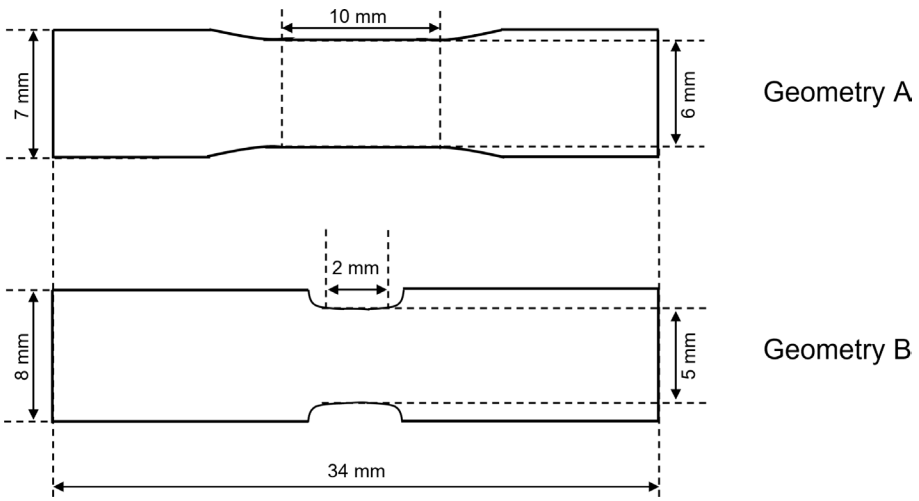

FIGURE 8 | Geometries of the dogbone-shaped specimen resulting from the punching process of the films. Geometry A is used for the ex situ analysis, and geometry B is used for the in situ IR analysis.

Figure 3a) the aromatic peak wavenumber $\nu_{C_1-C_4}$ is close to the initial value. The coloring of the pixels shows that mainly shear band domains contain stretched aromatic molecules as a result of the load-induced macroscopic deformation process. In the literature, Raman and IR peaks are analyzed for different materials under mechanical stress, for example, polyethylene or polypropylene, and the peak shift is attributed to a variation of bond lengths and angles [11, 62, 64] or a change in the molecular environment [65, 66]—we think that both happen at the same time but contribute differently for different chemical groups in the molecule, for example $C_1 - C_4$ or C—H in the aromatic ring, due to bond stretching (leading to a redshift) and polarization changes (leading to a blueshift) as will be explained later. Even if the *para*-phenylene group is a rigid and strongly bonded component in the backbone due to the π-electron systems, an increase of the bond lengths in the aromatic structure might be the cause of the redshift towards lower peak wavenumbers, as this can be demonstrated in the MD simulation as well (see Figure 7).

By reducing the film thickness to 15 µm, the absorbance of specific vibrational modes decreases in accordance with the Lambert–Beer law. This reduction enables the evaluation of additional peaks and vibrational modes. In Figure 9 the photoelastic image and the IR microscope results of a deformed epoxy film specimen with a thickness of 15 µm can be seen. Additionally, to the aromatic peak wavenumber values at 1608 cm^{-1}, in Figure 9 each pixel is colored regarding the peak shift of the peak wavenumber at 830 cm^{-1}. To assure the comparability of both peak shifts, the delta of the peak wavenumber of the specimen in relation to the peak wavenumber of unloaded specimens (initial state) is plotted and colored regarding the direction of peak shift. The peak at 830 cm^{-1} corresponds to an out-of-plane vibration of the aromatic hydrogen atoms ν_{C-H} [67, 68] and slightly shifts towards higher wavenumbers in the shear band regions, known as a blueshift. The absolute peak shift $\Delta\nu_{C-H}$ at 830 cm^{-1} is smaller than the peak shift $\Delta\nu_{C_1-C_4}$ at 1608 cm^{-1}. Since the aromatic C—H bonds are not integral to the main chain that directly experiences the applied load, the resulting peak shift is correspondingly less pronounced. Nevertheless, it can be seen that the peak $\Delta\nu_{C-H}$ slightly shifts to higher wavenumbers in the shear band regions of the deformed specimen.

The peak wavenumber at 830 cm^{-1} is assumed not only to be connected with the distance between the backbones, but may be also used as an indication for the intensity of inter-molecular forces as shown in the study of Doblies et al. [45]. An increase in the intensity of inter-molecular forces might lead to an increase peak wavenumber of the aromatic hydrogen bonds at 830 cm^{-1} due to a significant reduction of the distances between the polymeric backbones and a changed polarization.

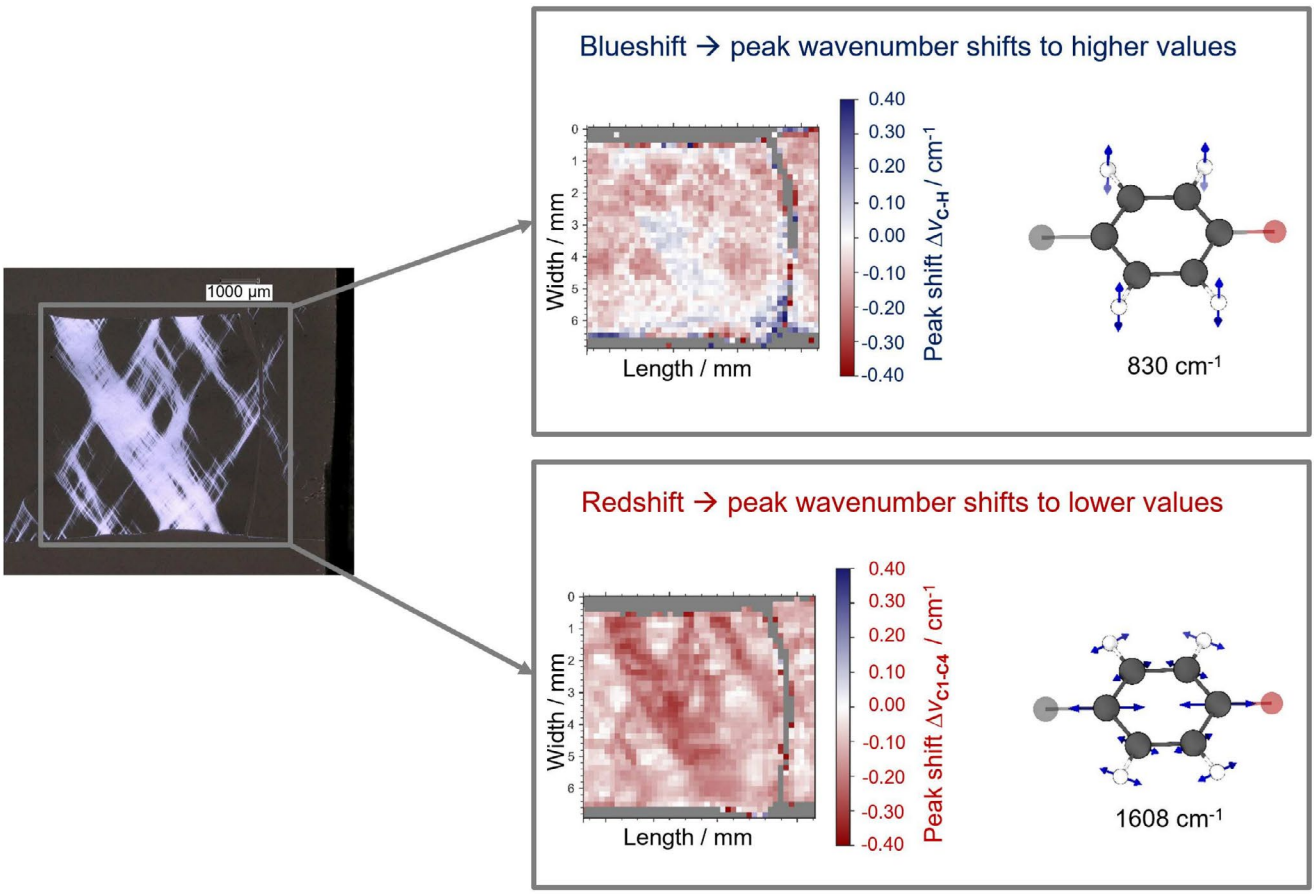

FIGURE 9 | Correlation of a photoelastic image and ex situ IR microscope results of a representative loaded film specimen with a thickness of 15 µm. Each pixel with a size of 165×165 µm is a measurement point and correspond to a spectrum. All recorded spectra are evaluated regarding the aromatic peak wavenumber $\nu_{C_1-C_4}$ and ν_{C-H}. Depending on the values of the peak shifts $\Delta\nu_{C_1-C_4}$ and $\Delta\nu_{C-H}$, each pixel is colored. Blue colored pixels correspond to a peak shift towards higher peak wavenumbers and red pixels show a decreased peak wavenumber compared to the initial peak wavenumber.

However, MD simulations have not observed a decrease in distance between the polymer chains or an increase in π–π interactions between the aromatic compounds deformation (see Figure 6 and Supporting Information: Section S1.4). Another, and maybe more plausible, explanation for the blueshift $\Delta\nu_{C-H}$ is that the stretching of the aromatic rings leads to changes in electron orbitals, thereby altering the vibrational energy of the aromatic hydrogen atoms. Hence, quantum mechanical computations are employed to obtain ab initio IR spectra for resin molecules. While molecular stretching due to mechanical deformation and consequently a redshift (cf. our previous discussion of the Badger's rule) is well-documented, the causes of the experimentally observed blueshift are yet not fully understood.

To capture the intricate phenomena of peak shifting, five distinct molecular configurations of BFDGE in vacuum are examined (Figure 10). The optimized structure of BFDGE (i) shows distances of 2.82 Å between the $C_1 - C_4$ atoms and 1.084 Å between the C—H atoms. The isolated elongation of the aromatic rings (ii) involves increasing the distance between anchor atoms by 0.05 to 5.75 Å, resulting in $C_1 - C_4$ distances of 2.85 Å while C—H distances remain at 1.084 Å. A single-linked BFDGE molecule between two DETDA moieties (iv) and the effect of stretching (v) are investigated. For the stretched configuration (vi), $\tilde{d}_0$ is increased by 1.2 to 23.8 Å, yielding $C_1 - C_4$ distances of 2.83 Å. The influence of π–π interactions (iii) is examined in both face–face and face–edge configurations. In the face–face configuration, aromatic rings are parallel at 5.6 Å, while in the face–edge configuration, they are perpendicular with a separation of 5.2 Å between their center of mass. Distances between $C_1 - C_4$ and C—H remain unchanged.

Gaussian broadening with a width of $\sigma = 2\,\mathrm{cm}^{-1}$ is applied to the data for peak identification. Vibrational displacement vectors, which represent the direction and magnitude of atomic movements during each vibrational mode, are inspected to ensure that these vibrations correspond to specific functional chemical groups and molecular domains. The centroid of each peak is calculated to assign wavenumbers to ν_{C1-C_4} and ν_{C-H}. Table 1 summarizes the distances and wavenumbers ν for the $C_1 - C_4$ and C—H vibrations across different configurations. Stretching along the main chain of the resin molecule (i → ii) causes a redshift in $C_1 - C_4$ wavenumbers, while out-of-plane C—H vibrations exhibit a blueshift compared to the relaxed structure (i).

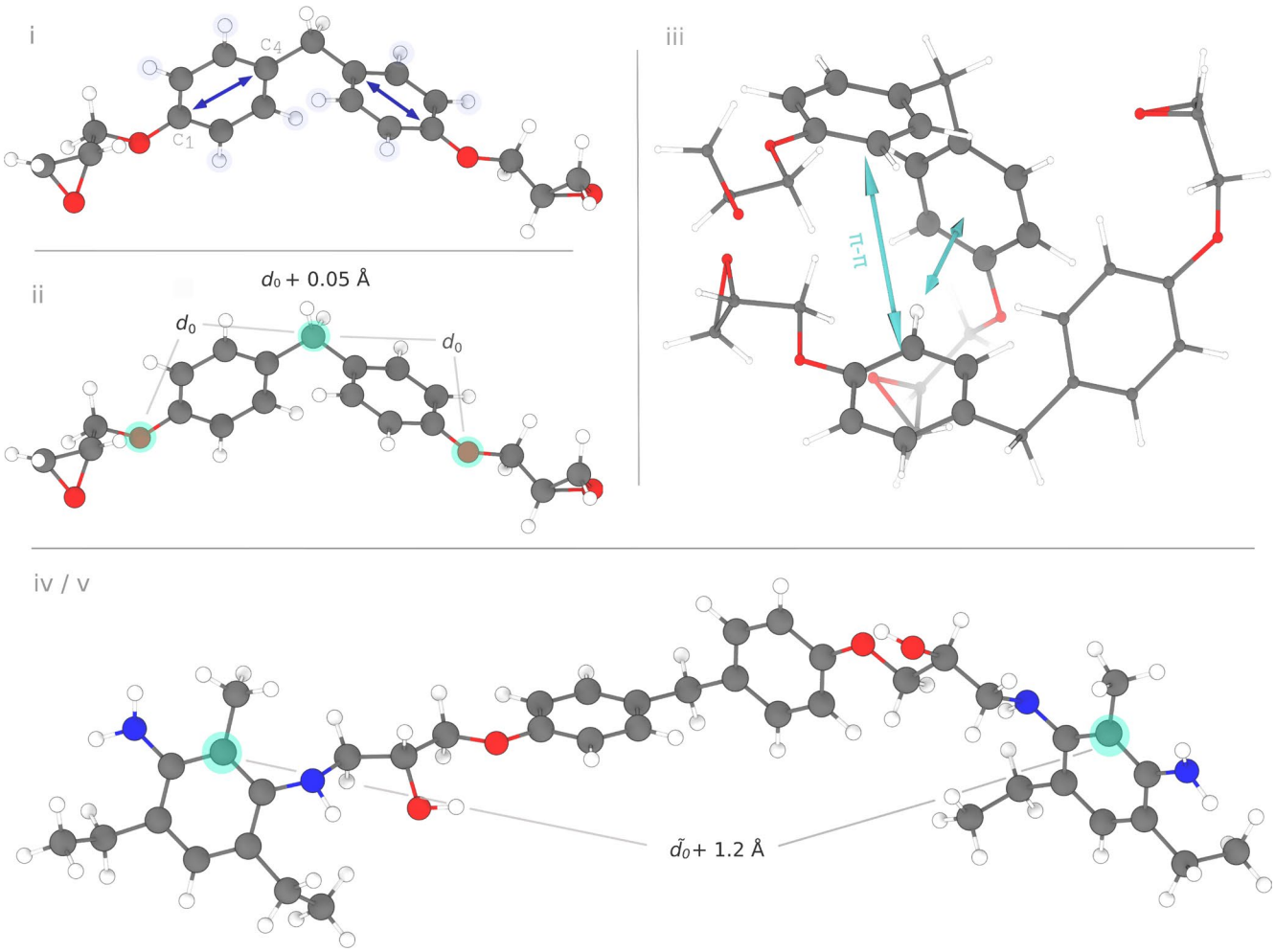

FIGURE 10 | To investigate the influence of deformation and the local molecular environment on the vibration of the $C_1 - C_4$ atoms of the aromatics in BFDGE (blue arrows), the IR spectra was computed for: (i) the relaxed structure, (ii) an elongation ($d_0 + 0.05$ Å) across the anchor atoms of the aromatics (highlighted in cyan), and (iii) BFDGE molecules involved in π–π interactions (highlighted by cyan arrows). Furthermore, a single-linked polymer chain of DETDA–BFDGE–DETDA (iv) was considered and its elongation (v) over the distance $\tilde{d}_0$, increased by 1.2 Å.

TABLE 1 | Quantum-mechanically calculated distances and wavenumbers (ν) for the IR spectra of $C_1 - C_4$ and C—H atoms for each molecular configuration (i–iii) of BFDGE molecules (B), single linked species to DETDA (D) (iv and v), and DGEBA (vi).

System	$\nu_{C_1-C_4}$ /cm^{-1}	ν_{C-H}/ cm^{-1}	$d_{C_1-C_4}$/Å	d_{C-H}/Å	Molecules
i	1650.2	815.0	2.82	1.084	B
ii	1638.2	815.3	2.85	1.084	B stretch
iii	1648.5	821.1	2.82	1.084	B + B
iv	1651.7	814.6	2.82	1.084	D–B–D
v	1645.8	816.1	2.83	1.084	D–B–D stretch
vi	1649.7	816.3	2.83	1.084	DGEBA

The influence of stretching on peak shifts in aromatic vibrations is also observed when comparing polymer chain elongation (iv → v), while preserving bond integrity.

Intermolecular interactions, such as π–π-bonds, influence the direction of the peak shifts as observed in the experiment. However, an increase in π–π interactions in the nm-sized model is not detected, which invalidates the assumption that peak shifts are due to π–π interactions. Additionally, DGBEA exhibits a spectral pattern similar to that of BFDGE, suggesting that DGBEA and BFDGE have comparable chemical and mechanical characteristics.

Overall, intra-molecular stretching, observed in configurations (ii) and (v), is identified as the primary factor inducing redshifts, in line with Badger's rule. The blueshift of the C—H vibration is thus most likely not correlated with bond length changes, suggesting an alternative mechanism. Analysis of Mulliken charges indicates that increased positive polarization of the aromatic hydrogen atoms in stretched molecules leads to higher vibrational frequencies, causing the observed blueshift. A more detailed discussion on the derivation of Mulliken charges and its interpretation with respect to polarization effects is provided in the Supporting Information: Section S1.2.

4 | Conclusions

This study has successfully elucidated the molecular mechanisms underlying macroscopic shear band formation in microscale epoxy film specimens. Through comprehensive experimental and computational investigations, including IR spectroscopy and molecular simulations, we revealed that shear bands manifest as oriented and stretched inhomogeneities within the epoxy material. These findings were substantiated through both in situ and ex situ IR measurements, as well as quantum and molecular mechanics simulations, enabling the correlation and tracking of molecular vibrations in response to mechanical loading and applied strain under various load conditions.

We introduced an ex situ IR microscopic technique to visualize molecular changes specifically within the shear band regions of loaded and deformed epoxy film samples, achieving high spatial resolution ($165 \times 165\ \mu m^2$). The resulting observations established a correlation between molecular backbone stretching and macroscopic shear band formation, as supported by molecular models that provide detailed insights into both polymer network and molecular strain.

The thin specimen thickness of only 15 μm allowed for the sensitive detection of a blueshift towards higher wavenumbers for the out-of-plane vibration of the hydrogen atoms bonded to the aromatic rings in the backbones ν_{C-H} within the formed shear bands. Quantum mechanical calculations indicated a stronger polarization for the C—H bond, leading to greater degrees of freedom and a stronger bond force constant for the associated vibration, thus explaining the experimentally and computationally observed blueshift of ν_{C-H}. In conclusion, two primary opposing mechanisms can cause a peak shift in vibrational spectra. First, bond stretching, in accordance with Badger's rule, results in a redshift. Second, bond polarization leads to a blueshift. It has been demonstrated that bond stretching has a more significant impact on the peak shift of the $C_1 - C_4$ vibration in the aromatic ring than polarization. Conversely, the polarization of the C—H bond induces a blueshift, as this bond is not part of the polymer backbone and thus remains constant in length. Furthermore, based on the methods employed, the impact of changes in free volume and the associated increase in π–π interactions on the observed blueshift behavior could not be determined, which contrasts with assumptions discussed in other studies [45].

By understanding the micromechanical behavior of epoxy resins at the molecular level, predictive modeling can be improved and thus ultimately the performance of FRPs in various industrial applications.

For future studies, we recommend polarized IR and Raman measurements to investigate load-induced molecular backbone orientations and the unraveling of entanglements in greater detail. Additionally, further decreasing the test volume of the epoxy film sample and utilizing a microtest device with a more precise load cell could provide deeper insights into stress fluctuations during mechanical loading as a result of molecular processes. These advancements will enhance the understanding of the relationship between molecular structure and macroscopic mechanical properties, paving the way for the development of next-generation composite materials with superior performance characteristics.

Acknowledgments

This research received funding from Grant No. 525597740 provided by the Deutsche Forschungsgemeinschaft (DFG, German Research Foundation). Publishing fees are supported by the Funding Programme Open Access Publishing of Hamburg University of Technology (TUHH).

Conflicts of Interest

The authors declare no conflicts of interest.

Data Availability Statement

The data that support the findings of this study are available on request from the corresponding author upon reasonable request.

References

1. O. Verschatse, L. Daelemans, W. V. Paepegem, and K. de Clerck, "In-Situ Observations of Microscale Ductility in a Quasi-Brittle Bulk Scale Epoxy," *Polymers* 12, no. 11 (2020): 2581, https://doi.org/10.3390/polym12112581.

2. F. A. Gilabert, D. Garoz, R. D. B. Sevenois, et al., "Composite Micro-Scale Model Accounting for Debonding, Strain-Rate Dependence and Damage Under Impact Using an Explicit Finite Element Solver." 17th European Conference on Composite Materials, 1–8, 2016.

3. T. J. Vaughan and C. T. McCarthy, "Micromechanical Modelling of the Transverse Damage Behaviour in Fibre Reinforced Composites," *Composites Science and Technology* 71, no. 3 (2011): 388–396.

4. W. Tan, F. Naya, L. Yang, et al., "The Role of Interfacial Properties on the Intralaminar and Interlaminar Damage Behaviour of Unidirectional Composite Laminates: Experimental Characterization and Multiscale Modelling," *Composites Part B: Engineering* 138 (2018): 206–221.

5. M.-F. Ren, X.-W. Zhang, C. Huang, B. Wang, and T. Li, "An Integrated Macro/Micro-Scale Approach for In Situ Evaluation of Matrix Cracking in the Polymer Matrix of Cryogenic Composite Tanks," *Composite Structures* 216 (2019): 201–212.

6. C. González and J. LLorca, "Multiscale Modeling of Fracture in Fiber-Reinforced Composites," *Acta Materialia* 54, no. 16 (2006): 4171–4181.

7. J. LLorca, C. González, J. M. Molina-Aldareguía, et al., "Multiscale Modeling of Composite Materials: A Roadmap Towards Virtual Testing," *Advanced Materials* 23, no. 44 (2011): 5130–5147.

8. L. Mishnaevsky, "Composite Materials for Wind Energy Applications: Micromechanical Modeling and Future Directions," *Computational Mechanics* 50, no. 2 (2012): 195–207.

9. E. Totry, J. M. Molina-Aldareguía, C. González, and J. LLorca, "Effect of Fiber, Matrix and Interface Properties on the In-Plane Shear Deformation of Carbon-Fiber Reinforced Composites," *Composites Science and Technology* 70, no. 6 (2010): 970–980.

10. R. P. Wool, "Mechanisms of Frequency Shifting in the Infrared Spectrum of Stressed Polymers," *Journal of Polymer Science: Part B: Polymer Physics* 13 (1975): 1795–1808.

11. A. Sturcová, S. J. Eichhorn, and M. C. Jarvis, "Vibrational Spectroscopy of Biopolymers Under Mechanical Stress: Processing Cellulose Spectra Using Bandshift Difference Integrals," *Biomacromolecules* 7, no. 9 (2006): 2688–2691.

12. W.-Y. Yeh and R. J. Young, "Molecular Deformation Processes in Aromatic High Modulus Polymer Fibres," *Polymer* 40, no. 4 (1999): 857–870.

13. C. Galiotis, I. M. Robinson, R. J. Young, B. J. E. Smith, and D. N. Batchelder, "Strain Dependence of the Raman Frequencies of a Kevlar 49 Fibre," *Polymer Communications* 26, no. 12 (1985): 354–355.

14. S. van der Zwaag, M. G. Northolt, R. J. Young, I. M. Robinson, C. Galiotis, and D. N. Batchelder, "Chain Stretching in Aramid Fibers," *Polymer Communications* 28 (1987): 276–277.

15. R. J. Young, R. J. Day, and M. Zakikhami, "The Structure and Deformation Behaviour of Poly(p-Phenylene Benzobisoxazole) Fibres," *Journal of Materials Science* 25 (1990): 127–136.

16. C. Galiotis and D. N. Batchelder, "Strain Dependences of the First- and Second-Order Raman Spectra of Carbon Fibres," *Journal of Materials Science Letters* 7, no. 5 (1988): 545–547.

17. I. M. Robinson, M. Zakikhani, R. J. Day, R. J. Young, and C. Galiotis, "Strain Dependence of the Raman Frequencies for Different Types of Carbon Fibres," *Journal of Materials Science Letters* 6, no. 10 (1987): 1212–1214.

18. W.-Y. Yeh and R. J. Young, "Deformation Processes in Poly(Ethylene Terephthalate) Fibers," *Journal of Macromolecular Science, Part B* 37, no. 1 (1998): 83–118.

19. S. J. Eichhorn, J. Sirichaisit, and R. J. Young, "Deformation Mechanisms in Cellulose Fibres, Paper and Wood," *Journal of Materials Science* 36, no. 36 (2001): 3129–3135.

20. S. J. Eichhorn, R. J. Young, and W.-Y. Yeh, "Deformation Processes in Regenerated Cellulose Fibers," *Textile Research Journal* 71, no. 2 (2001): 121–129.

21. A. Sturcová, G. R. Davies, and S. J. Eichhorn, "Elastic Modulus and Stress-Transfer Properties of Tunicate Cellulose Whiskers," *Biomacromolecules* 6, no. 2 (2005): 1055–1061.

22. B. Hinterstoisser, M. Akerholm, and L. Salmén, "Load Distribution in Native Cellulose," *Biomacromolecules* 4, no. 5 (2003): 1232–1237.

23. P. Peetla, K. C. Schenzel, and W. Diepenbrock, "Determination of Mechanical Strength Properties of Hemp Fibers Using Near-Infrared Fourier Transform Raman Microspectroscopy," *Applied Spectroscopy* 60, no. 6 (2006): 682–691.

24. J. Sirichaisit, V. L. Brookes, R. J. Young, and F. Vollrath, "Analyis of Structure/Property Relationships in Silkworm (*Bombyx mori*) and Spider Dragline (*Nephila edulis*) Silks Using Raman Spectroscopy," *Biomacromolecules* 4, no. 2 (2003): 387–394.

25. J. Sirichaisit, R. J. Young, and F. Vollrath, "Molecular Deformation in Spider Dragline Silk Subjected to Stress," *Polymer* 41 (2000): 1223–1227.

26. S. J. Eichhorn and R. J. Young, "Deformation Micromechanics of Natural Cellulose Fibre Network and Composites," *Composites Science and Technology* 63, no. 9 (2003): 1225–1240.

27. C. Galiotis, R. J. Young, P. H. J. Yeung, and D. N. Batchelder, "The Study of Model Polydiacetylene/Epoxy Composites, Part 1 the Axial Strain in the Fibre," *Journal of Materials Science* 19, no. 11 (1984): 3640–3648.

28. I. M. Robinson, R. J. Young, C. Galiotis, and D. N. Batchelder, "Study of Model Polydiacetylene/Epoxy Composites, Part 2 Effect of Resin Shrinkage," *Journal of Materials Science* 22, no. 10 (1987): 3642–3646.

29. R. J. Young, R. J. Day, M. Zakikhani, and I. M. Robinson, "Fibre Deformation and Residual Thermal Stresses in Carbon Fibre Reinforced Peek," *Composites Science and Technology* 34, no. 3 (1989): 243–258.

30. C. Galiotis, N. Melanitis, D. N. Batchelder, I. M. Robinson, and J. A. Peacock, "Residual Strain Mapping in Carbon Fibre/Peek Composites," *Composites* 19, no. 4 (1988): 321–324.

31. V. Varshney, S. S. Patnaik, A. K. Roy, and B. L. Farmer, "A Molecular Dynamics Study of Epoxy-Based Networks: Cross-Linking Procedure and Prediction of Molecular and Material Properties," *Macromolecules* 41, no. 18 (2008): 6837–6842.

32. N. Nouri and S. Ziaei-Rad, "A Molecular Dynamics Investigation on Mechanical Properties of Cross-Linked Polymer Networks," *Macromolecules* 44, no. 13 (2011): 5481–5489.

33. R. H. Meißner, J. Konrad, B. Boll, B. Fiedler, and D. Zahn, "Molecular Simulation of Thermosetting Polymer Hardening: Reactive Events Enabled by Controlled Topology Transfer," *Macromolecules* 53, no. 22 (2020): 9698–9705.

34. B. Arash, W. Exner, and R. Rolfes, "A Viscoelastic Damage Model for Nanoparticle/Epoxy Nanocomposites at Finite Strain: A Multiscale Approach," *Journal of the Mechanics and Physics of Solids* 128 (2019): 162–180.

35. J. Konrad, S. Pfaller, and D. Zahn, "Multi-Scale Modelling of Plastic Deformation, Damage and Relaxation in Epoxy Resins," *Polymers* 14, no. 16 (2022): 3240.

36. B. Koo, N. Subramanian, and A. Chattopadhyay, "Molecular Dynamics Study of Brittle Fracture in Epoxy-Based Thermoset Polymer," *Composites Part B: Engineering* 95 (2016): 433–439.

37. J. Konrad, R. H. Meißner, E. Bitzek, and D. Zahn, "A Molecular Simulation Approach to Bond Reorganization in Epoxy Resins: From Curing to Deformation and Fracture," *ACS Polymers Au* 1, no. 8 (2021): 165–174.

38. J. Konrad and D. Zahn, "Bottom-To-Top Modeling of Epoxy Resins: From Atomic Models to Mesoscale Fracture Mechanisms," *Journal of Chemical Physics* 160, no. 2 (2024): 024111.

39. O. Büyüköztürk, M. J. Buehler, D. Lau, and C. Tuakta, "Structural Solution Using Molecular Dynamics: Fundamentals and a Case Study of Epoxy-Silica Interface," *International Journal of Solids and Structures* 48, no. 14–15 (2011): 2131–2140.

40. A. Shokuhfar and B. Arab, "The Effect of Cross Linking Density on the Mechanical Properties and Structure of the Epoxy Polymers: Molecular Dynamics Simulation," *Journal of Molecular Modeling* 19, no. 9 (2013): 3719–3731.

41. J. Konrad, P. Moretti, and D. Zahn, "Molecular Simulations and Network Analyses of Surface/Interface Effects in Epoxy Resins: How Bonding Adapts to Boundary Conditions," *Polymers* 14, no. 19 (2022): 4069.

42. A. A. Bahraq, M. A. Al-Osta, I. B. Obot, O. S. Baghabra Al-Amoudi, T. A. Saleh, and M. Maslehuddin, "Improving the Adhesion Properties of Cement/Epoxy Interface Using Graphene-Based Nanomaterials: Insights From Molecular Dynamics Simulation," *Cement and Concrete Composites* 134 (2022): 104801.

43. J. Konrad and D. Zahn, "Interfaces in Reinforced Epoxy Resins: From Molecular Scale Understanding Towards Mechanical Properties," *Journal of Molecular Modeling* 29, no. 8 (2023): 243.

44. J. Mittelhaus, P. Röttger, E. Schill, J. Jacobs, and B. Fiedler, "Investigation of the Ductile Deformation Potential of Microscale Epoxy Materials," *Polymer Testing* 128 (2023): 108217.

45. A. Doblies, B. Fiedler, T. Würger, E. Schill, H. R. Meißner, and C. Feiler, "Mechanical Degradation Estimation of Thermosets by Peak Shift Assessment: General Approach Using Infrared Spectroscopy and Atomistic Simulations," *Polymer* 221 (2021): 123585.

46. M. J. Frisch, G. W. Trucks, H. B. Schlegel, et al., "Gaussian 09 Revision A.2," 2009.

47. W. L. Jorgensen, D. S. Maxwell, and J. Tirado-Rives, "Development and Testing of the Opls All-Atom Force Field on Conformational Energetics and Properties of Organic Liquids," *Journal of the American Chemical Society* 118, no. 45 (1996): 11225–11236.

48. K. H. Nicastro, C. J. Kloxin, and T. H. Epps, "Potential Lignin-Derived Alternatives to Bisphenol a in Diamine-Hardened Epoxy Resins," *ACS Sustainable Chemistry & Engineering* 6, no. 11 (2018): 14812–14819.

49. J. Konrad and D. Zahn, "Assessing the Mechanical Properties of Molecular Materials From Atomic Simulation," *AIMS Materials Science* 8 (2021): 867–880.

50. D. Zahn, B. Schilling, and S. M. Kast, "Enhancement of the Wolf Damped Coulomb Potential: Static, Dynamic, and Dielectric Properties of Liquid Water From Molecular Simulation," *Journal of Physical Chemistry B* 106, no. 41 (2002): 10725–10732.

51. C. J. Fennell and J. D. Gezelter, "Is the Ewald Summation Still Necessary? Pairwise Alternatives to the Accepted Standard for Long-Range Electrostatics," *Journal of Chemical Physics* 124, no. 23 (2006): 234104, https://doi.org/10.1063/1.2206581.

52. A. P. Thompson, H. M. Aktulga, R. Berger, et al., "Lammps—A Flexible Simulation Tool for Particle-Based Materials Modeling at the Atomic, Meso, and Continuum Scales," *Computer Physics Communications* 271 (2022): 108171.

53. D. J. Evans and B. L. Holian, "The Nose–Hoover Thermostat," *Journal of Chemical Physics* 83, no. 8 (1985): 4069–4074.

54. G. W. Ehrenstein, *Polymer Werkstoffe: Struktur-Eigenschaften-Anwendung*, 3rd ed. (Carl Hanser, 2011).

55. W. Retting, *Mechanik der Kunststoffe: Die mechanischen Eigenschaften von Polymer-Werkstoffen* (Carl Hanser, 1992).

56. P. R. Griffiths and J. A. Haseth, *Fourier Transform Infrared Spectrometry*, 2nd ed. (John Wiley & Sons, 2007).

57. R. M. Badger, "A Relation Between Internuclear Distances and Bond Force Constants," *Journal of Chemical Physics* 2, no. 3 (1934): 128–131.

58. R. M. Badger, "The Relation Between Internuclear Distances and the Force Constants of Diatomic Molecules," *Physical Review* 48, no. 3 (1935): 284–285.

59. R. M. Badger, "The Relation Between the Internuclear Distances and Force Constants of Molecules and Its Application to Polyatomic Molecules," *Journal of Chemical Physics* 3, no. 11 (1935): 710–714.

60. R. P. Wool, "Measurements of Infrared Frequency Shifts in Stressed Polymers," *Journal of Polymer Science: Part B: Polymer Physics* 19 (1981): 449–457.

61. N. Gierlinger, M. Schwanninger, A. Reinecke, and I. Burgert, "Molecular Changes During Tensile Deformation of Single Wood Fibers Followed by Raman Microscopy," *Biomacromolecules* 7, no. 7 (2006): 2077–2081.

62. J. M. Chalmes, M. W. Mackenzie, and H. A. Willis, "Ftir Spectroscopic Studies of Isotactic Polypropylene Films Under Stress," *Spectrochimica Acta* 47, no. 12 (1991): 1677–1683.

63. E. Kraka, J. A. Larsson, and D. Cremer, "Generalization of the Badger Rule Based on the Use of Adiabatic Vibrational Modes." 2010.

64. T. Kida, Y. Hiejima, and K. Nitta, "Raman Spectroscopic Study of High-Density Polyethylene During Tensile Deformation," *International Journal of Experimental Spectroscopic Techniques* 1, no. 1 (2016): 1–6.

65. A. A. Profit, V. Felsen, J. Chinwong, E.-R. E. Mojica, and R. Z. B. Desamero, "Evidence of π-Stacking Interactions in the Self-Assembly of Hiapp(22-29)," *Proteins* 81, no. 4 (2013): 690–703.

66. E. M. Cabaleiro-Lago and J. Rodríguez-Otero, "On the Nature of σ-σ, σ-π, and π-π Stacking in Extended Systems," *ACS Omega* 3, no. 8 (2018): 9348–9359.

67. D. Lin-Vien, N. B. Colthup, W. G. Fateley, and J. G. Grasselli, *The Handbook of Infrared and Raman Characteristic Frequencies of Organic Molecules* (Academic Press, 1991).

68. N. Colthup, L. H. Daly, and S. E. Wiberley, *Introduction to Infrared and Raman Spectroscopy*, 3rd ed. (Academic Press, 1990).

Supporting Information

Additional supporting information can be found online in the Supporting Information section.